

VIP Very Important Paper

www.batteries-supercaps.org

Electrolyte-free cathode design for solid-state batteries demonstrated with bifunctional Li_2VCl_4

Takuma Kasahara,^[a] Peng Song,^[a] Itaru Honma,^[a] and Saneyuki Ohno^{*[a]}

All-solid-state batteries have attracted much attention because of the expected high energy density and inherent safety stemming from their nonflammable property. While improving the energy density of the cathode poses a significant challenge, here we introduce a novel battery design strategy to enhance energy density by employing bifunctional cathode material, allowing the weight ratio of the active material to be increased without using an electrolyte for the cathode. By employing lithium-containing vanadium halide Li_2VCl_4 , serving as both active material and electrolyte, the all-solid-state battery cell with no electrolyte for the cathode with a capacity approaching the theoretical limit is demonstrated. In addition, we present a

guideline for improving capacity retention from the perspective of interfacial stability. Notably, thermodynamic analysis revealed interfacial instability between Li_2VCl_4 and sulfide material. A double-layer separator, incorporating halide materials for the cathode side, was implemented to enhance the interfacial stability and mitigate the capacity degradation. Furthermore, it was found that the rate capability depends on the lithium content in synthesized $\text{Li}_{2-x}\text{VCl}_4$ and does not change with the state of charge significantly. This study will contribute to designing the bifunctional cathode material for an all-solid-state battery and describe its unique properties.

1. Introduction

Batteries, indispensable for harnessing energy in diverse applications, are experiencing rapidly growing demand in today's increasingly electrified world. Lithium-ion batteries are now widely used as rechargeable batteries with greater energy density to meet the growing demand for applications in electric vehicles (EVs) and energy storage technology.^[1] Generally, battery cathodes comprise active material, electrolytes, and conductivity aids, as shown in Figure 1(a). Among the components, the active material is responsible for storing energy; therefore, the loading capacity of the active material in the cathode directly determines the battery's energy density.^[2] Conventional lithium-ion batteries utilize liquid electrolytes and solid cathode active materials, which are fundamentally distinct from one another. This necessitates sparing certain fractions of the cathode for liquid electrolytes and virtually limits the weight ratio of the active material in the cathode.

In recent years, the development of solid-state ionic conductors, or solid electrolytes, has progressed significantly,^[3–6] and all-solid-state batteries, which are composed entirely of solid-state materials, are increasingly attracting attention due to their potential for higher safety and energy efficiency for next-generation batteries.^[7] In all-solid-state batteries where both the

electrolyte and the cathode active material are solid states, the concept of bifunctional cathode materials, serving as both electrolyte and active material, is applicable.^[8–10] Bifunctional cathode materials do not require electrolytes in the cathode because they are active materials that function as electrolytes (Figure 1b). Therefore, if made properly, employing bifunctional cathode materials is expected to realize an "electrolyte-free" cell design that drastically increases the ratio of active material in the cathode, thereby improving the energy density.

In this study, lithium-containing metal halides are considered suitable candidates for realizing bifunctional cathode materials. The essential properties of bifunctional cathode materials include ionic conductivity, reversible redox reactions, and electrochemical stability against potential changes associated with redox reactions. Among ion-conductive solids, sulfide-based materials such as $\text{Li}_6\text{PS}_5\text{X}$ ($\text{X}=\text{Cl}, \text{Br}, \text{I}$),^[11–13] Li_3PS_4 ,^[14,15] and $\text{Li}_{10}\text{GeP}_2\text{S}_{12}$,^[16–18] have been known for high ionic conductivity, and oxide-based materials such as $\text{Li}_3\text{La}_7\text{Zr}_2\text{O}_{12}$,^[19,20] $\text{Li}_{1+x}\text{Al}_x\text{Ti}_{2-x}(\text{PO}_4)_3$,^[21–23] and $\text{Li}_x\text{PO}_y\text{N}_z$ ^[24] have been known for high electrochemical stability. The two main types of solid electrolytes, sulfides and oxides, each face distinct challenges: sulfides have issues with electrochemical stability,^[7] and oxides have issues with ionic conductivity.^[7] In contrast, lithium-ion conducting halides, attracting increased attention in recent years, possess both high ionic conductivity and electrochemical stability.^[25–28] These characteristics align with the functions required for bifunctional cathode materials. Therefore, lithium-containing metal halides are explored as promising candidate materials for bifunctional cathode materials. Among the lithium-containing metal halides, Li_2VCl_4 has been reported to have ionic conductivity in previous studies,^[29–31] and considering that vanadium halides were recently considered as promising cathode materials,^[32,33] Li_2VCl_4 is picked up as the model material.

[a] T. Kasahara, P. Song, I. Honma, S. Ohno

Institute of Multidisciplinary Research for Advanced Materials, Tohoku University, 2-1-1 Katahira, Aoba-ku, Sendai, Miyagi 980-8577, Japan
E-mail: saneyuki.ohno.c8@tohoku.ac.jp Supporting information for this article is available on the WWW under <https://doi.org/10.1002/batt.202400520> © 2024 The Authors. *Batteries & Supercaps* published by Wiley-VCH GmbH. This is an open access article under the terms of the Creative Commons Attribution License, which permits use, distribution and reproduction in any medium, provided the original work is properly cited.

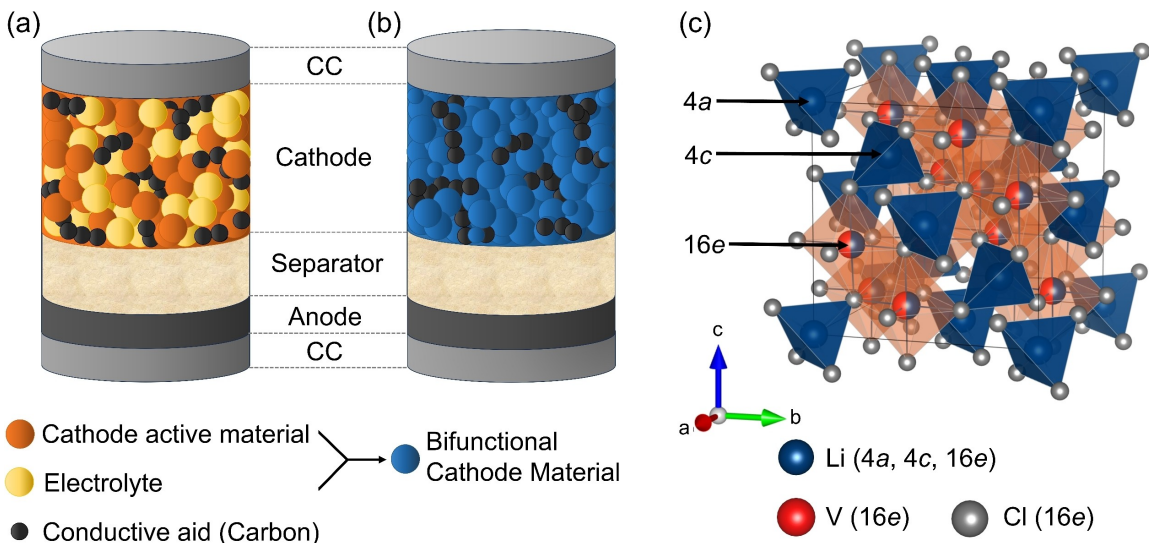
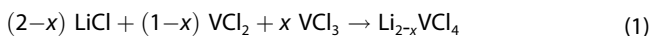


Figure 1. (a) The schematic of the architecture of conventional batteries with no binders. CC stands for the current collector. (b) The schematic of the cell with bifunctional cathode materials. (c) The crystal structure of Li_2VCl_4 with the space group of F 4 3 m.

A successful development of a bifunctional cathode material that combines the functionalities of both cathode active material and electrolyte by using Li_2VCl_4 is demonstrated in this study. The transport properties and redox reaction mechanism of Li_2VCl_4 were investigated by synthesizing the materials in various states of charge, $\text{Li}_{2-x}\text{VCl}_4$, and applying them to all-solid-state battery cathodes. Then, the investigation focused on the cause of capacity degradation, analyzing them from the viewpoint of interfacial stability. By addressing this problem, we significantly improved the battery life. We also clarified the peculiar characteristic of bifunctional cathode materials, which is that variation in the synthesis stoichiometry affects the charge-discharge characteristics. This study provides a new strategy to improve the energy density of batteries.

Methods

Synthesis: The five stoichiometric points of the chemical state $\text{Li}_{2-x}\text{VCl}_4$ ($x=0, 0.25, 0.5, 0.75, 1$) were synthesized. All samples were mechanochemically synthesized under argon atmospheres. LiCl 99.9% (Kojundo), VCl_2 85% (Fuji Film), and VCl_3 97% (Sigma Aldrich) were used as starting materials. The formula of synthesis is below.



A stoichiometric mixture of starting materials was filled into ZrO_2 cups with a 30:1 mass ratio for 5 mm ZrO_2 balls, then the ball-milling was conducted using PULVERISETTE7 (Fritsch GmbH) with the setting of 500 rpm for 99 cycles (each cycle consists of 15 minutes of milling and 5 minutes of pause).

Synchrotron powder X-ray diffraction (XRD): Phase identification was carried out using the beamline BL02B2 at SPring-8 in Japan. The powder samples were housed in a Lindemann capillary tube with an inner diameter 0.3 mm. The wavelength used for the measurement was determined to be 0.413965(4) Å by calibrating

using CeO_2 as a standard sample. The measurement results were refined by Pawley fitting using TOPAS-Academic V7 software^[34] to identify the lattice constant. Crystal structures were visualized by VESTA software package.^[35] To thoroughly investigate the interfacial stability of $\text{Li}_{2-x}\text{VCl}_4$ within all-solid-state batteries, we performed the temperature-dependent synchrotron powder XRD on the mixture of Li_2VCl_4 and LiVCl_4 with $\text{Li}_6\text{PS}_5\text{Cl}$ and Li_3YCl_6 . The samples were sealed in a Borosilicate capillary tube with an inner diameter of 0.3 mm, and the temperature was changed from 300 K to 673 K.

Scanning electron microscopy (SEM): The surface morphology of the samples was examined using JSM-7800F (JEOL Ltd.) under 15 kV and 1 Å. Prior to SEM analysis, the samples were carefully prepared to ensure proper imaging. The powdered samples were first mounted on copper stubs using carbon tape to ensure good electrical contact. All images were captured at multiple magnifications to assess both the overall structure and finer morphological details of the sample. The voltage and current are 15 kV and 11 A, respectively. Energy Dispersive X-ray Spectroscopy (EDS) was performed in conjunction with SEM to map the elemental distribution.

Ionic conductivity measurement: The ionic transport properties of the synthesized samples were evaluated by temperature-dependent electrochemical impedance spectroscopy, ranging from -30 to 60 °C, and the direct current (DC) polarization measurement. For Impedance spectroscopy, 150 mg sample powder was filled into an airtight press cell (ø10 mm) and pressed by two cylindric stainless steel bars. After the cell was assembled, a pressure of 300 MPa was applied to stainless steel bars for 3 minutes. The stainless-steel frame maintained a 60 MPa pressure during the measurement. The electrochemical measurements were performed on Celltest System 1470E (SOLATRON ANALYTICAL) impedance analyzer using a 10 mV voltage amplitude with frequencies ranging from 1 MHz to 100 mHz. The cell was placed in a climate chamber to control its temperature during testing. The RelaxIS3 software was used to fit the obtained impedance data. DC polarization measurement to confirm the ionic transport was performed on symmetric cells with electron-blocking electrodes configured as In/InLi | $\text{Li}_6\text{PS}_5\text{Cl}$ | $\text{Li}_{2-x}\text{VCl}_4$ | $\text{Li}_6\text{PS}_5\text{Cl}$ | In/InLi. 80 mg of $\text{Li}_{2-x}\text{VCl}_4$ sample powder was filled into an airtight cell and compressed by two cylindric stainless steel bars at 100 MPa. After pressing 80 mg of $\text{Li}_6\text{PS}_5\text{Cl}$ was filled into both sides of the cell. Subsequently, a pressure of 300 MPa was

applied to for 3 minutes. Then $\phi 9$ mm indium foil (100 μm thick) and $\phi 6$ mm Li foil (120 μm thick) were placed on both sides of the cell to establish a lithium-ion source and drain. The constructed cell was then placed in the cell holder to keep a pressure of 60 MPa during the measurement. Six different voltages (250, 150, 50, -100, -200, -300 mV) were applied to the cell, and each voltage was held for 2 hours to relax the measured current. The total ionic resistance was calculated from the slope of the I-V curve. The resistance of $\text{Li}_{2-x}\text{VCl}_4$ was obtained by subtracting the resistance of $\text{Li}_6\text{PS}_5\text{Cl}$ from the total resistance. The resistance of $\text{Li}_6\text{PS}_5\text{Cl}$ was calculated by impedance spectroscopy like $\text{Li}_{2-x}\text{VCl}_4$. The DC ionic conductivity of $\text{Li}_{2-x}\text{VCl}_4$ was calculated from the resistance and thickness of pellets calculated from the relative density of pressed $\text{Li}_{2-x}\text{VCl}_4$.

Cell construction and electrochemical measurement: Synthesized $\text{Li}_{2-x}\text{VCl}_4$ and carbon (Ketjenblack) were mixed in mortar for 15 minutes with a 9:1 mass ratio, and it was used as a cathode composite. $\text{Li}_6\text{PS}_5\text{Cl}$ and Li_3YCl_6 were used as separators. In-Li alloy was used as an anode (0 V vs. In/InLi corresponds to 0.62 V vs. Li^+/Li).^[36] Two types of all-solid-state battery cells were constructed. One is with a single-layer separator that uses only $\text{Li}_6\text{PS}_5\text{Cl}$ for the separator; the configuration is ($\text{Li}_{2-x}\text{VCl}_4$) (8 mg) | $\text{Li}_6\text{PS}_5\text{Cl}$ (80 mg) | In/InLi. The other one is the double-layer separator, which used Li_3YCl_6 for the separator of the cathode side and $\text{Li}_6\text{PS}_5\text{Cl}$ for the anode side. The configuration is ($\text{Li}_{2-x}\text{VCl}_4$ -C) (8 mg) | Li_3YCl_6 (60 mg) | $\text{Li}_6\text{PS}_5\text{Cl}$ (60 mg) | In/InLi. The separator was filled in a tight cell and compressed with 100 MPa by stainless bars. After that, the cathode composite was filled in the cell and compressed with 300 MPa for 3 minutes. Finally, $\phi 9$ mm indium foil (100 μm thick) and $\phi 6$ mm Li foil (120 μm thick) were installed on both sides of the cell. A pressure of 60 MPa is applied during the measurement. The stainless-steel bars were used as current collectors. Battery cells were cycled on HJI1020mSD8 (Hokuto Denko). The dQ/dV was calculated as $\Delta(\text{Ah})/\Delta V$ where ΔV is the change in the capacity of a cell and ΔV is the change in cell voltage as a result of $\Delta(\text{Ah})$. Further smoothing of dQ/dV was accomplished by using a moving average in 10 mV to make the dQ/dV plot. The state of charge (SOC)-dependent impedance spectroscopy was also conducted.^[37,38] The detailed procedure is in the Supplementary Information. For SOC-dependent Impedance spectroscopy, a slightly thicker cathode with 16 mg was employed to clearly separate the resistance component of the cathode in the analysis.

2. Results and Discussion

2.1. Characterization

The properties of $\text{Li}_{2-x}\text{VCl}_4$ were obtained from a structural viewpoint. Li_2VCl_4 has a cubic structure (space group of $F\bar{4}3m$) as shown in Figure 1c. In this structure, lithium occupies three sites: two on the tetrahedral sites (Wyckoff 4a and 4c) and the other one on the octahedral sites (Wyckoff 16e). Vanadium occupies only octahedral sites (Wyckoff 16e), sharing with lithium, with each element occupying half of these positions. First, materials with the stoichiometric composition of $\text{Li}_{2-x}\text{VCl}_4$ ($x=0, 0.25, 0.5, 0.75, 1$) were synthesized by ball milling. Scanning electron spectroscopy (SEM) and Electron dispersive X-ray spectroscopy (EDS) for synthesized LiVCl_4 and Li_2VCl_4 (Figure S1) indicated the homogeneous distribution of V and Cl. The synchrotron X-ray diffraction pattern of the synthesized $\text{Li}_{2-x}\text{VCl}_4$ is shown in Figure 2(a). Despite their broadened peaks, the

peak positions are in good agreement with the theoretical XRD pattern of F 4 3 m- Li_2VCl_4 . No impurity peaks were observed in all samples. Figure 2(b) and Figure S2 show the results of the Pawley fitting, and the lattice constants obtained from the fittings are shown in Figure 2(c). The lattice constants increase with the lithium contents. It can be considered that this is simply because the amount of lithium in the structure influences the lattice constant. The Li_2VCl_4 peaks in the $\text{Li}_{2-x}\text{VCl}_4$ with no impurity peak and monotonic change in the lattice size indicate the lithium de-insertion mechanism in the Li_2VCl_4 structure between V^{2+} and V^{3+} .

The ionic transport properties of the synthesized samples $\text{Li}_{2-x}\text{VCl}_4$ ($x=0, 0.25, 0.5, 0.75, 1$) were characterized using DC polarization measurements and temperature-dependent impedance spectroscopy. For DC polarization, the electron-blocking resistance of In/InLi | $\text{Li}_6\text{PS}_5\text{Cl}$ | $\text{Li}_{2-x}\text{VCl}_4$ | $\text{Li}_6\text{PS}_5\text{Cl}$ | In/InLi symmetric cell was measured, and the ionic conductivity of $\text{Li}_{2-x}\text{VCl}_4$ was calculated by subtracting the resistance of $\text{Li}_6\text{PS}_5\text{Cl}$ from total resistance. The I-V plot for DC polarization measurement is shown in Figure S3. For impedance spectroscopy, the Nyquist plot was fitted by an equivalent circuit, as shown in Figure 2(d) and Figure S3. The ionic conductivity was calculated based on ionic resistance obtained from fitting, ranging from 1.0 to $3.0 \times 10^{-5} \text{ S cm}^{-1}$, with each composition exhibiting different ionic conductivities (Figure 2(e)). The conductivities from DC and impedance agree well.

2.2. Cycle Performance

To assess the electrochemical behavior of $\text{Li}_{2-x}\text{VCl}_4$ synthesized with different Li contents, the cell cycling performance was examined with a constant current in an all-solid-state battery configuration. $\text{Li}_{2-x}\text{VCl}_4$ and carbon were mixed at a weight ratio of 9:1 as a bifunctional cathode. As for the separator, $\text{Li}_6\text{PS}_5\text{Cl}$ was employed to avoid the electrolyte reduction on the anode side, which utilizes In/InLi (0.62 V vs. Li^+/Li). This cell configuration is referred to as a single-layer cell hereafter. As shown in Figure 3(a), the observed initial discharged capacity changes linearly to lithium contents in $\text{Li}_{2-x}\text{VCl}_4$. At this point, the redox equilibrium can be expected as below.



Figure 3(a) also compares the initial discharge capacities of $\text{Li}_{2-x}\text{VCl}_4$ ($x=0, 0.25, 0.5, 0.75, 1$) with the theoretical capacities estimated according to the expected redox equilibrium (2). Namely, with the theoretical initial discharge capacity of Li_2VCl_4 of 129.7 mAh g^{-1} , the theoretical value of the initial discharge capacity of $\text{Li}_{2-x}\text{VCl}_4$ is calculated as $129.7 \times x \text{ mAh g}^{-1}$. As shown in Figure 3(a), the initial discharge capacity was in great agreement with the theoretical value, corroborating the expected redox reaction as equation (1) in $\text{Li}_{2-x}\text{VCl}_4$. This also confirms that the functional cathode is obtainable only with $\text{Li}_{2-x}\text{VCl}_4$ and carbon; Li_2VCl_4 is a bifunctional cathode material that has functions of both active material and electrolyte.

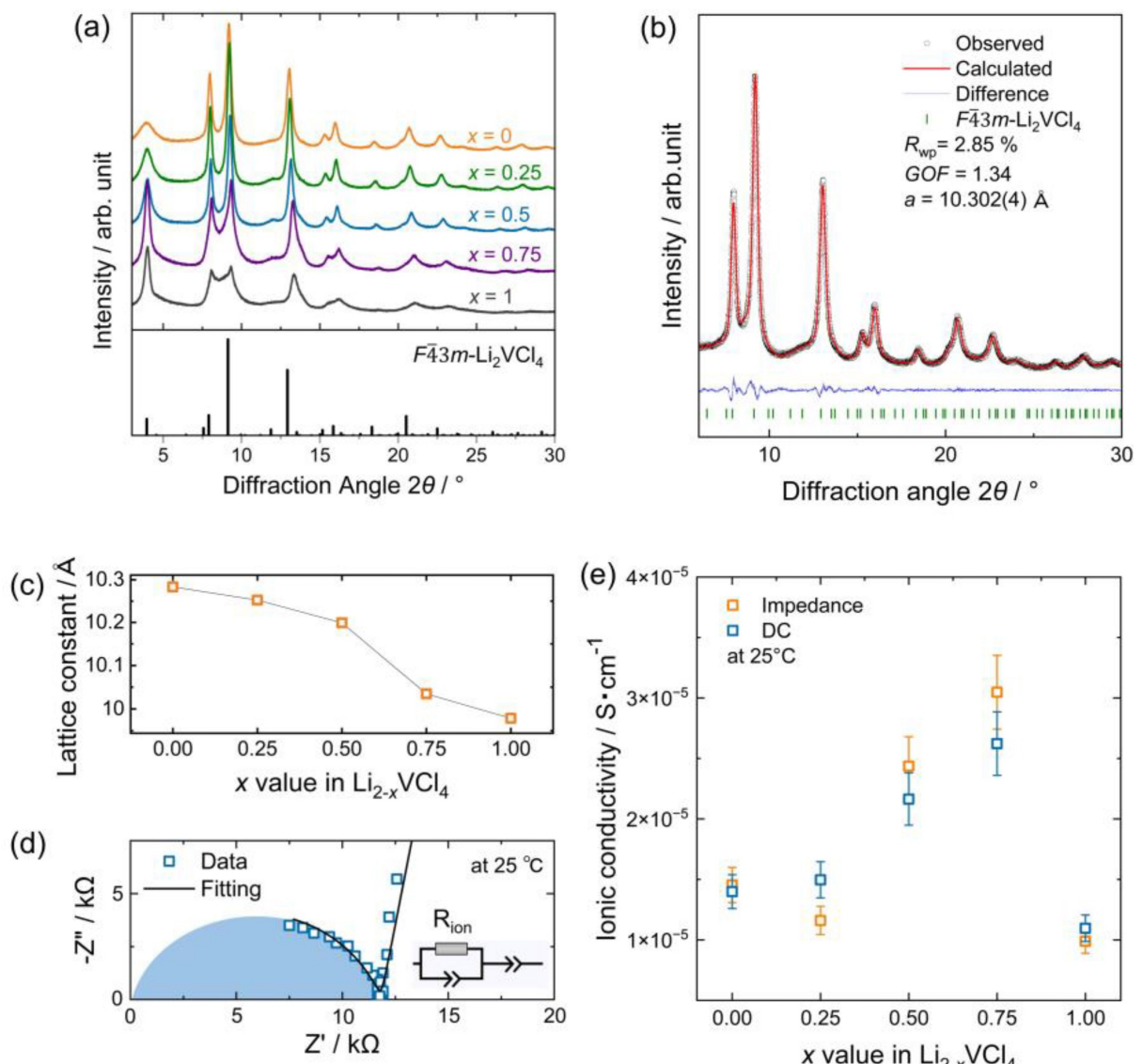


Figure 2. (a) The synchrotron X-ray diffraction pattern of $\text{Li}_{2-x}\text{VCl}_4$ ($x = 0, 0.25, 0.5, 0.75, 1$) with the reference pattern of $F\bar{4}3m\text{-Li}_2\text{VCl}_4$.^[39] (b) Representative Pawley fitting for synchrotron X-ray diffraction of Li_2VCl_4 . GOF means the goodness of fit. (c) The lattice constants of $\text{Li}_{2-x}\text{VCl}_4$ ($x = 0, 0.25, 0.5, 0.75, 1$) obtained from the Pawley fitting. (d) The representative Nyquist plot of impedance spectroscopy for LiVCl_4 at 25°C and equivalent circuit used for fitting. (e) The ionic conductivity of $\text{Li}_{2-x}\text{VCl}_4$ ($x = 0, 0.25, 0.5, 0.75, 1$) measured by DC polarization and impedance spectroscopy.

To further understand the cyclability of the here-obtained bifunctional cathode material, the capacity retention of Li_2VCl_4 and LiVCl_4 was examined and shown in Figure 3(b). Figure S4 shows the potential profiles and cycling efficiencies of the cells. The initial capacity reached approximately 85 % of the theoretical capacity (129.7 mAh g^{-1}), but after 50 cycles, the capacity of the cell using LiVCl_4 and Li_2VCl_4 decreased by 22.2 % and 31.4 %, respectively. It was necessary to clarify the reasons for capacity degradation to improve cycle properties.

2.3. Interfacial Stability

A potential cause of capacity degradation was identified as the interfacial instability between $\text{Li}_{2-x}\text{VCl}_4$ and the solid electrolyte

$\text{Li}_6\text{PS}_5\text{Cl}$, which was used as a separator. In addition to the limited electrochemical stability of the sulfide electrolytes,^[40-41] several recent studies indicate chemical instability at the interface between ion-conducting halides such as Li_3InCl_6 and sulfide ion conductors, e.g., $\text{Li}_6\text{PS}_5\text{Cl}$.^[42-44] Although the stability between halide-based cathode and sulfide electrolytes has not been explored to the best of our knowledge, an analogous degradation mechanism could potentially cause the stability issues of the interface between $\text{Li}_{2-x}\text{VCl}_4$ and $\text{Li}_6\text{PS}_5\text{Cl}$.

To gain a hint of the interfacial stability among the cathode components, temperature-dependent XRD measurements were performed on a mixture of $\text{Li}_{2-x}\text{VCl}_4$ and $\text{Li}_6\text{PS}_5\text{Cl}$ to determine whether the two materials can coexist in a thermodynamically stable state. The reaction that possibly occurs at the interface in the cycling environment can be visualized by accelerating the

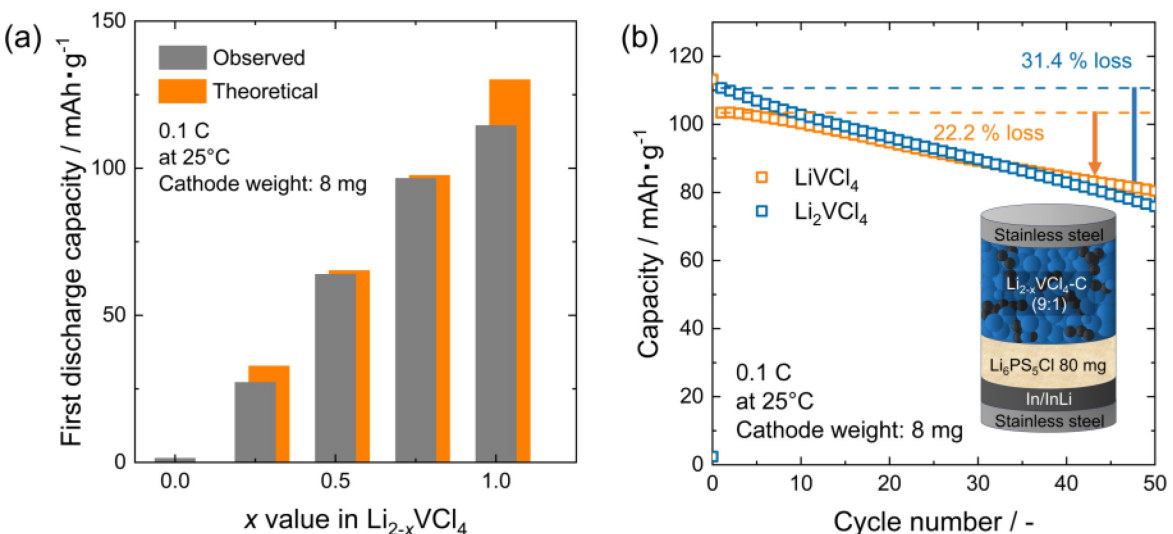
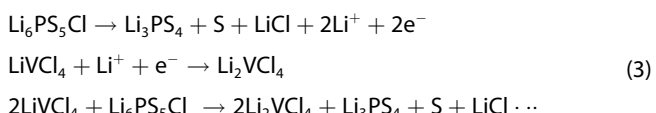


Figure 3. The cycle properties of $\text{Li}_{2-x}\text{VCl}_4 - \text{C} \mid \text{Li}_6\text{PS}_5\text{Cl} \mid \text{In}/\text{InLi}$ cells. (a) The initial-discharge capacity of the cells and its theoretical value. The theoretical capacity is given by $x \times 129.7 \text{ mAh g}^{-1}$. (b) The discharge capacity of the cells using LiVCl_4 and Li_2VCl_4 as cathode. The numbers show the percentage of capacity loss after 50 cycles.

reaction between the two materials at high temperatures. Furthermore, to assess the stability of the interface between $\text{Li}_{2-x}\text{VCl}_4$ and another solid electrolyte, we conducted similar experiments using Li_3YCl_6 , which is expected to be electrochemically stable. In the temperature-dependent XRD of the mixture of $\text{LiVCl}_4\text{-Li}_6\text{PS}_5\text{Cl}$ and $\text{Li}_2\text{VCl}_4\text{-Li}_6\text{PS}_5\text{Cl}$ shown in Figure 4(a) and (b), the disappearance of the $\text{Li}_6\text{PS}_5\text{Cl}$ below 550 K and around 600 K, respectively, coincided with the emergence of $\beta\text{-Li}_3\text{PS}_4$ and LiCl peaks (the appearance of these peaks is highlighted in Figure S5). In contrast, the Li_3YCl_6 peak did not disappear at higher temperatures in the mixture with LiVCl_4 and Li_2VCl_4 , as shown in Figure 4(b) and (d).

These results suggest a clear electrochemical degradation of $\text{Li}_6\text{PS}_5\text{Cl}$ with LiVCl_4 and a possible chemical reaction with Li_2VCl_4 . As for the electrochemical degradation, the disappearance of the $\text{Li}_6\text{PS}_5\text{Cl}$ peak at high temperatures, coupled with the appearance of the $\beta\text{-Li}_3\text{PS}_4$ and LiCl peaks, suggests that the following reaction pathway may occur at the interface between these materials.



As shown in the chemical equation, the reaction proceeds by the decomposition of $\text{Li}_6\text{PS}_5\text{Cl}$, generating lithium ions that migrate to LiVCl_4 , which, in turn, forms the Li_2VCl_4 . Considering the discharge potential of LiVCl_4 (2.3 V vs. In/InLi) being well above the stability of argyrodite (1.7 V vs. In/InLi), this reaction can lead to the formation of less ion-conductive interphases.^[42]

Whereas the degradation pathway mentioned above is evident, we propose another possible degradation hiding behind the intense electrochemical reaction, a chemical reaction between the halides and sulfides. Although the mixture of

$\text{Li}_2\text{VCl}_4\text{-Li}_6\text{PS}_5\text{Cl}$ shows slightly higher thermal stability, the decomposition of the $\text{Li}_6\text{PS}_5\text{Cl}$ is observed far below its decomposition/melting temperature $> 873 \text{ K}$ (solid-state reaction is typically conducted at 823 K), indicating the onset of the reaction between $\text{Li}_2\text{VCl}_4\text{-Li}_6\text{PS}_5\text{Cl}$.^[45] Based on the recent report exploring the interface between Li_3InCl_6 and $\text{Li}_6\text{PS}_5\text{Cl}$ through time-of-flight secondary ion mass spectroscopy, the onset of the anion exchange reaction was confirmed by detecting InS^- .^[40] Samanta and the team further explored the mechanistic understanding and revealed that such instability correlates with the electronegativity of the central cation in halides. Based on their argument, In^{3+} and Zr^{4+} are the two most reactive central cations, and V^{3+} has even higher electronegativity, suggesting an even more intense interfacial reaction.^[43]

In contrast to the case with sulfide electrolytes, the decomposition of Li_3YCl_6 did not occur. In summary, the interface between $\text{Li}_{2-x}\text{VCl}_4$ and $\text{Li}_6\text{PS}_5\text{Cl}$ may become unstable during cycling, likely leading to the decomposition of $\text{Li}_6\text{PS}_5\text{Cl}$ even at room temperature, and the interface between $\text{Li}_{2-x}\text{VCl}_4$ and Li_3YCl_6 was found to be more stable. Therefore, the instability at the interface between $\text{Li}_{2-x}\text{VCl}_4$ and $\text{Li}_6\text{PS}_5\text{Cl}$ is most likely the cause of significant capacity degradation in $(\text{Li}_{2-x}\text{VCl}_4\text{-C}) \mid \text{Li}_6\text{PS}_5\text{Cl} \mid \text{In}/\text{InLi}$ cells.

To address the interfacial instability between the cathode and separator, a double-layer cell configuration was implemented by introducing an additional separator layer of Li_3YCl_6 . As illustrated in Figure 5(a), the separator structure comprised a Li_3YCl_6 layer adjacent to the cathode side and a $\text{Li}_6\text{PS}_5\text{Cl}$ layer for the anode side. The electrochemical cycling tests conducted on the double-layer cells, as depicted in Figure 5(b), demonstrate a significant enhancement in capacity retention, with the capacity loss after 50 cycles being approximately 50% lower than that observed in the single-layer cell for both LiVCl_4 and Li_2VCl_4 cathodes. The charge-discharge property is shown in Figure S6. The voltage profiles of the cells with $\text{Li}_{2-x}\text{VCl}_4$ are

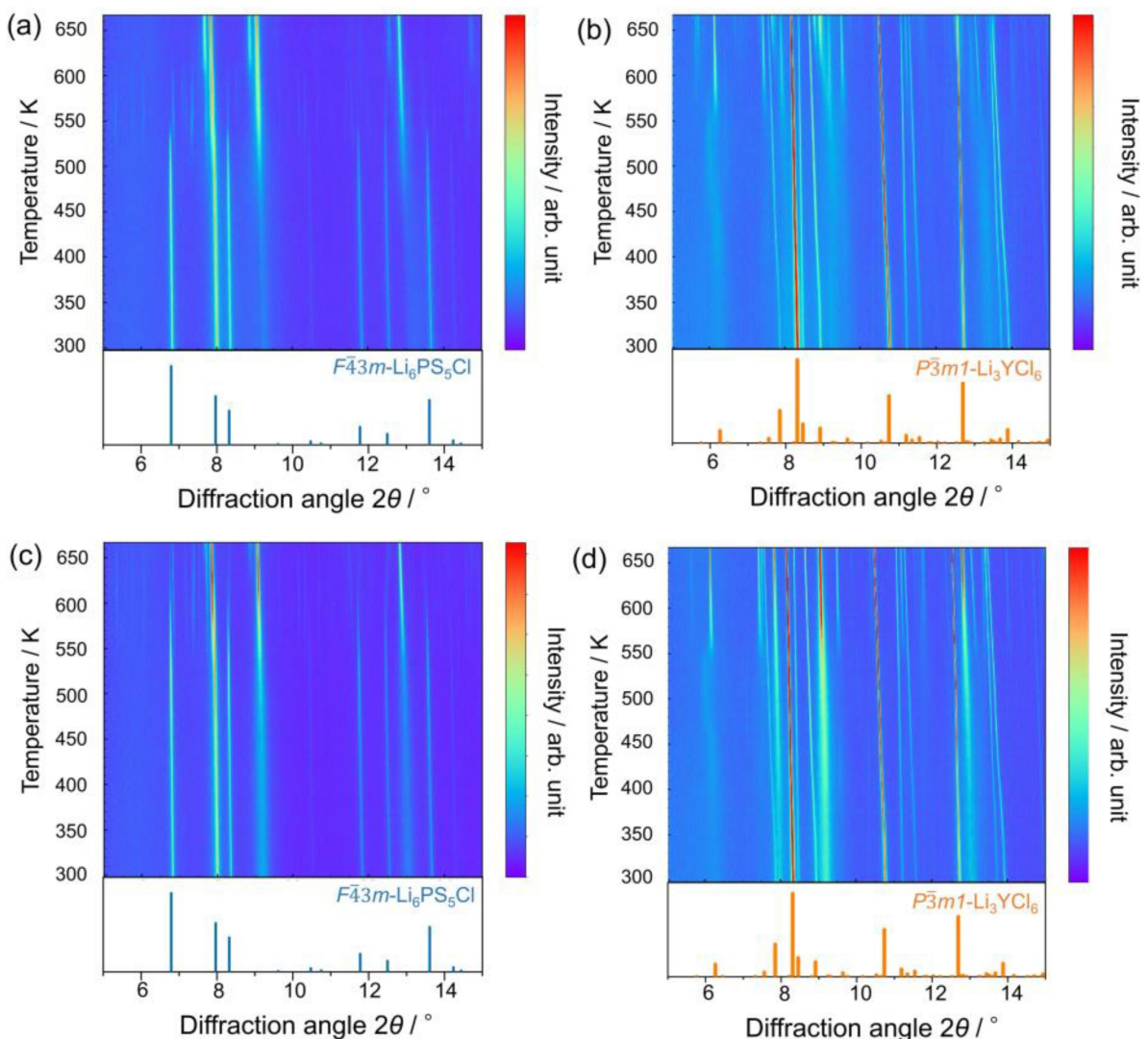


Figure 4. The color maps of temperature-dependent synchrotron XRD for various components: (a) LiVCl_4 – $\text{Li}_6\text{PS}_5\text{Cl}$, (b) LiVCl_4 – Li_3YCl_6 , (c) Li_2VCl_4 – $\text{Li}_6\text{PS}_5\text{Cl}$, (d) Li_2VCl_4 – Li_3YCl_6 . Temperature ranged from 300 K to 673 K. The graphs below temperature-dependent graphs show simulated reference XRD peaks of $\text{Li}_6\text{PS}_5\text{Cl}$ and Li_3YCl_6 , respectively.

shown in Figure 5(c). Consistent with the findings discussed in Figure 4(b) and (d), Li_3YCl_6 exhibits minimal reactivity with $\text{Li}_{2-x}\text{VCl}_4$, suggesting that the double-layer separator effectively inhibits the reaction between $\text{Li}_{2-x}\text{VCl}_4$ and $\text{Li}_6\text{PS}_5\text{Cl}$ with suppressed evolution of the cell overpotentials, thereby substantially extending the battery life. These results underscore the critical importance of cathode-separator interfacial stability in determining the cycle life of the battery.

2.4. Composition-Dependent Charge-Discharge and Ionic Transport in $\text{Li}_{2-x}\text{VCl}_4$ Solid-State Batteries

In addition to battery performance being influenced by interface stability, we also found that the performance varies depending on the nominal composition of the synthesized cathode material. The differential capacity (dQ/dV) plots in Figure S7 reveal distinct differences in the redox potentials

between the cells containing LiVCl_4 and Li_2VCl_4 . The first discharge profiles show peak positions at 2.18 V and 2.22 V for LiVCl_4 and Li_2VCl_4 , respectively. The initial difference in the redox potential likely reflects the local structural difference.

Two possible scenarios are the following. In the reported Li_2VCl_4 structure, vanadium only occupies the sites octahedrally coordinated by chlorines (Wyckoff 16e), and lithium can take the tetrahedral coordination (Wyckoff 4a and 4c). By reducing the lithium contents in the nominal composition, the lattice parameters of the synthesized samples decrease monotonically while keeping the space group of the structure (Figure 2). This suggests the formation of lithium vacancies concurrent with an increase in V^{3+} content. Given the smaller ionic radius of V^{3+} compared to V^{2+} (0.64 Å versus 0.79 Å in octahedral coordination), the increased V^{3+} content may result in partial occupation of lithium sites, thereby explaining the observed differences in redox potentials between samples with varying nominal compositions. The non-linear changes in lattice constants may

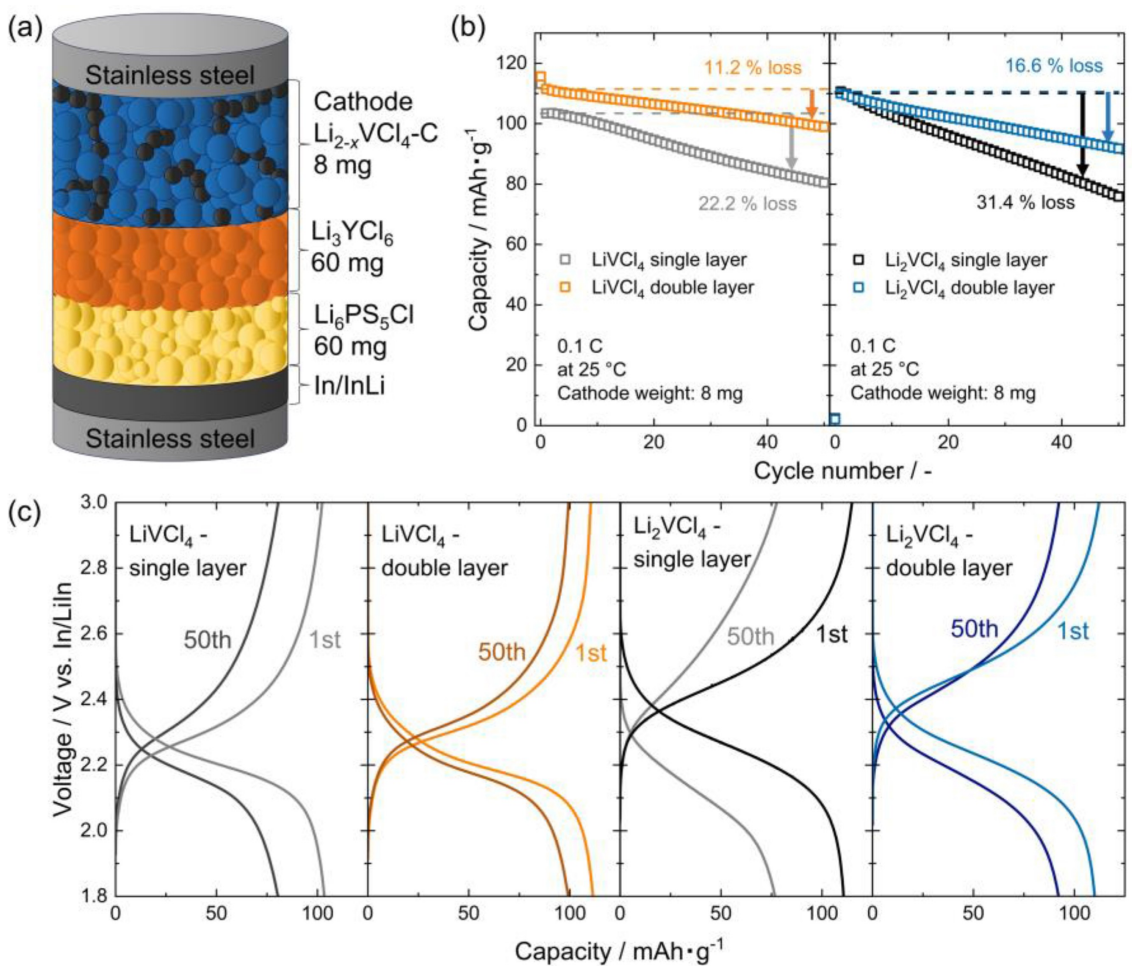


Figure 5. (a) Schematic of the double-layer cell structure. (b) The capacity retention of single and double layers with LiVCl_4 and Li_2VCl_4 . (c) The voltage profiles for single- and double-layer cells for LiVCl_4 and Li_2VCl_4 .

further support the existence of complex local structural variations. The second possibility involves forming glass phases with distinct local structural frameworks compared to the crystalline phase. Notably, upon cycling, the initially higher redox potential of Li_2VCl_4 gradually decreases until the difference between the two cells becomes negligible after 50 cycles, with both showing the peak positions of 2.17 V. X-ray analysis also reveals a progressive peak broadening with decreasing lithium contents, lending support to this scenario. However, definitive experimental or theoretical evidence for the hypothesis remains elusive, primarily due to the challenges in performing reliable Rietveld refinement on low-crystallinity samples and conducting detailed local structural analysis of glass phases mixed with fine crystalline phases. Further investigation is needed to elucidate these structural evolution mechanisms and definitively determine the relationship between composition, local structure, and electrochemical performance.

Furthermore, state of charge (SOC) dependent impedance spectroscopy was performed on double-layer cells to monitor how the ion transport property of the cathode changes. The impedance spectra obtained from the cell at various SOCs were fitted with the equivalent circuit shown in Figure 6(b), where

R_{CT} represents the resistance from charge transfer, R_{off} represents the resistance from other elements, including the separators and wirings, and W represents the Warburg coefficient reflecting carrier diffusion. The following analysis was conducted upon the first charging after the initial discharge of the cells. The effective ionic conductivity, σ_{ion}^{eff} , was determined from $R_{c,ion}$, calculated by subtracting the separator contributions from the R_{off} as shown below.

$$R_{c,ion} = R_{off} - R_{LPSC} - R_{LYC}$$

R_{LPSC} and R_{LYC} represent the resistance of the $\text{Li}_6\text{PS}_5\text{Cl}$ and Li_3YCl_6 layer, respectively. Notably, with the double amount of cathode loading, $R_{c,ion}$ becomes double as expected from the cathode contribution (see also Figure S8). Figure 6(c) shows σ_{ion}^{eff} and R_{CT} obtained from SOC-dependent impedance spectroscopy for the cells with LiVCl_4 and $\text{Li}_{1.5}\text{VCl}_4$. While the change in R_{CT} is prominent around the SOC of 0% and 100%, R_{CT} remains almost constant during charging. The effective ionic conductivity σ_{ion}^{eff} also remains more or less the same with a slight reduction as the SOC increases. This is likely due to the decreased number of mobile carriers in the structure. Impor-

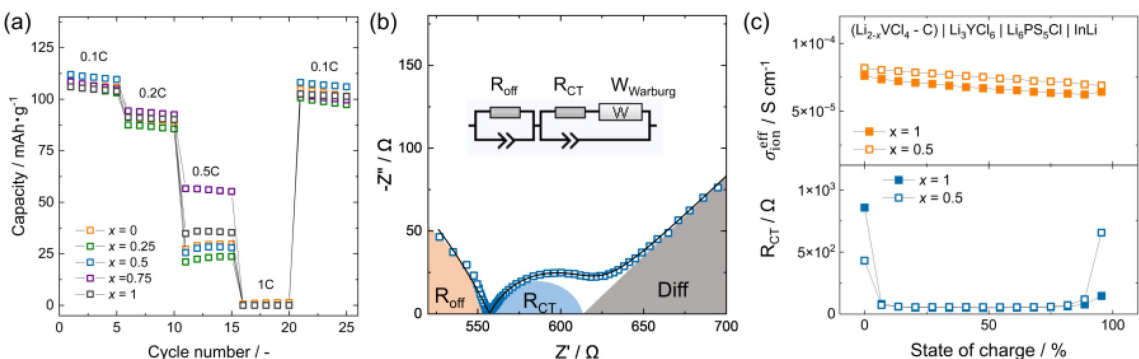


Figure 6. (a) The rate characteristics of $\text{Li}_{2-x}\text{VCl}_4\text{-C} \mid \text{Li}_3\text{YCl}_6 \mid \text{Li}_6\text{PS}_5\text{Cl} \mid \text{In}/\text{InLi}$ cell, indicating the discharge capacity at each rate (0.1 C, 0.2 C, 0.5 C, and 1 C). (b) The represented Nyquist curve was obtained from SOC-dependent impedance spectroscopy, and the equivalent circuit used for fitting. R_{CT} represents the resistance from charge transfer, and R_{off} is the resistance from the other elements, including the separators and wirings. (c) The plot of $\sigma_{\text{ion}}^{\text{eff}}$ and R_{CT} obtained from SOC dependent impedance spectroscopy with different cathode weight.

tantly, even with a drastic change in the charge state and the associated change in the carrier density, $\text{Li}_{2-x}\text{VCl}_4$ holds the essential property as the bifunctional cathode material, a robust ionic conductivity during its redox activity. It should also be noted that $\sigma_{\text{ion}}^{\text{eff}}$ of $\text{Li}_{1.5}\text{VCl}_4$ is higher than that of LiVCl_4 , as expected from the bulk ionic conductivity shown in Figure 2.

From these observations, we found that the ion transport of $\text{Li}_{2-x}\text{VCl}_4$ can significantly vary depending on the nominal composition for the synthesis; however, once the structure, likely the anion sublattice, is fixed, the ion transport property does not change drastically during the charging or discharging. This suggests the critical importance of initial composition and the anion framework in the active material to design better-performing bifunctional cathode materials.

3. Conclusions

We present a novel strategy to improve the energy density of battery cathodes by developing a bifunctional cathode material, lithium-containing vanadium $\text{Li}_{2-x}\text{VCl}_4$, which concurrently serves as an electrolyte and active material. The employment of $\text{Li}_{2-x}\text{VCl}_4$ in all-solid-state battery cells demonstrated effective rechargeability and achieved a capacity approaching its theoretical limit. Furthermore, we identified the cause of capacity degradation as the instability between the cathode material, $\text{Li}_{2-x}\text{VCl}_4$, and the sulfide-based separator, $\text{Li}_6\text{PS}_5\text{Cl}$. This issue was mitigated by applying a double-layer separator composed of Li_3YCl_6 and $\text{Li}_6\text{PS}_5\text{Cl}$, establishing interfacial stability between the cathode and the separator and significantly reducing energy loss during battery cycling. Furthermore, the unique property of the bifunctional cathode material, which is that the synthesized composition influences ionic transportation and charge-discharge properties, was clarified. This work provides valuable insights into the design and characteristics of bifunctional cathode materials.

Supporting Information

The supporting information is available free of charge.

SEM-EDS images; synchrotron XRD pattern of synthesized $\text{Li}_{2-x}\text{VCl}_4$ with Pawley fittings; information about the temperature-impedance spectroscopy; information about the DC polarization measurement; charge-discharge curve, Coulombic efficiency, and conversion efficiency for single-layer cell; comparison of temperature-dependent XRD pattern before and after decomposition of $\text{Li}_6\text{PS}_5\text{Cl}$; charge-discharge curve, Coulombic efficiency, and conversion efficiency for double-layer cell; dQ/dV plots of double-layer cell configuration; detailed procedure of SOC-dependent impedance spectroscopy; and comparison of Nyquist plots obtained from SOC-dependent impedance spectroscopy with different cathode weight.

Notes

The authors declare no competing financial interest.

Acknowledgements

S.O. gratefully acknowledges Toyota Riken for financial support through a Rising Fellow Program. This research was supported by the JSPS KAKENHI Grant Numbers JP23K26762. The synchrotron radiation experiments were performed at the BL02B2 of SPring-8 with the approval of the Japan Synchrotron Radiation Research Institute (JASRI) (Proposal Nos. 2024A1505).

Conflict of Interests

The authors declare no conflict of interest.

Data Availability Statement

The data that support the findings of this study are available from the corresponding author upon reasonable request.

- [1] M. Li, J. Lu, Z. Chen, K. Amine, *Adv. Mater.* **2018**, *30*, 1521–4095.
[2] A. Manthiram, *ACS Cent. Sci.* **2017**, *3*, 1063–1069.
[3] T. Famprikis, P. Canepa, J. A. Dawson, M. S. Islam, C. Masquelier, *Nat. Mater.* **2019**, *18*, 1278–1291.
[4] X. He, Y. Zhu, Y. Mo, *Nat. Commun.* **2017**, *8*, 15893.
[5] S. Ohno, A. Banik, G. F. Dewald, M. A. Kraft, T. Krauskopf, N. Minafra, P. Till, M. Weiss, W. G. Zeier, *Progress in Energy* **2020**, *2*, 022001.
[6] W. Kou, Y. Zhang, W. Wu, Z. Guo, Q. Hua, J. Wang, *Green Energy and Environment* **2024**, *9*, 71–80.
[7] T. Schmaltz, F. Hartmann, T. Wicke, L. Weymann, C. Neef, J. Janek, *Adv. Energy Mater.* **2023**, *43*, 2301886.
[8] T. Shigedomi, Y. Fujita, T. Kishi, K. Motohashi, H. Tsukasaki, H. Nakajima, S. Mori, M. Tatsumisago, A. Sakuda, A. Hayashi, *Chem. Mater.* **2022**, *34*, 9745–9752.
[9] T. Shigedomi, Y. Fujita, K. Motohashi, M. Tatsumisago, A. Sakuda, A. Hayashi, *ACS Appl. Mater. Interfaces* **2024**, *16*, 20542–20550.
[10] N. Tanibata, N. Nonaka, K. Makino, H. Takeda, M. Nakayama, *Sci. Rep.* **2024**, *14*, 2703.
[11] S. Ohno, B. Helm, T. Fuchs, G. Dewald, M. A. Kraft, S. P. Culver, A. Senyshyn, W. G. Zeier, *Chem. Mater.* **2019**, *31*, 4936–4944.
[12] N. Minafra, M. A. Kraft, T. Bernges, C. Li, R. Schlem, B. J. Morgan, W. G. Zeier, *Inorg. Chem.* **2020**, *59*, 11009–11019.
[13] M. A. Kraft, S. Ohno, T. Zinkevich, R. Koerver, S. P. Culver, T. Fuchs, A. Senyshyn, S. Indris, B. J. Morgan, W. G. Zeier, *J. Am. Chem. Soc.* **2018**, *140*, 16330–16339.
[14] Z. Liu, W. Fu, E. A. Payzant, X. Yu, Z. Wu, N. J. Dudney, J. Kiggans, K. Hong, A. J. Rondinone, C. Liang, *J. Am. Chem. Soc.* **2013**, *135*, 975–978.
[15] K. Homma, M. Yonemura, T. Kobayashi, M. Nagao, M. Hirayama, R. Kanno, *Solid State Ion.* **2011**, *182*, 53–58.
[16] Y. Kato, S. Hori, R. Kanno, *Adv. Energy Mater.* **2020**, *10*, 2002153.
[17] S. P. Culver, A. G. Squires, N. Minafra, C. W. F. Armstrong, T. Krauskopf, F. Böcher, C. Li, B. J. Morgan, W. G. Zeier, *J. Am. Chem. Soc.* **2020**, *142*, 21210–21219.
[18] T. Krauskopf, S. P. Culver, W. G. Zeier, *Chem. Mater.* **2018**, *30*, 1791–1798.
[19] M. Rosen, R. Ye, M. Mann, S. Lobe, M. Finsterbusch, O. Guillou, D. Fattakhova-Rohlfing, *J. Am. Chem. Soc.* **2021**, *9*, 4831–4840.
[20] L. Buannic, B. Orayech, J. M. López Del Amo, J. Carrasco, N. A. Katcho, F. Aguesse, W. Manalastas, W. Zhang, J. Kilner, A. Llordés, *Chem. Mater.* **2017**, *29*, 1769–1778.
[21] R. DeWees, H. Wang, *ChemSusChem* **2019**, *12*, 3713–3725.
[22] F. Ma, E. Zhao, S. Zhu, W. Yan, D. Sun, Y. Jin, C. Nan, *Solid State Ion.* **2016**, *295*, 7–12.
[23] M. Illbeigi, A. Fazlali, M. Kazazi, A. H. Mohammadi, *Solid State Ion.* **2016**, *289*, 180–187.
[24] V. Lacivita, N. Artrith, G. Ceder, *Chem. Mater.* **2018**, *30*, 7077–7090.
[25] T. Asano, A. Sakai, S. Ouchi, M. Sakaida, A. Miyazaki, S. Hasegawa, *Adv. Mater.* **2018**, *30*, 1803075.
[26] S. Wang, Q. Bai, A. M. Nolan, Y. Liu, S. Gong, Q. Sun, Y. Mo, *Angew. Chem.* **2019**, *131*, 8123–8127.
[27] Y. Nikodimos, W. N. Su, B. J. Hwang, *Adv. Energy Mater.* **2023**, *13*, 202202854.
[28] B. Tao, D. Zhong, H. Li, G. Wang, H. Chang, *Chem. Sci.* **2023**, *14*, 8693–8722.
[29] C. Cros, L. Hanebali, L. Lati, rard Villeneuve, W. Gang, *Solid State Ion.* **1983**, *9–10*, 139–147.
[30] J. L. Soubeyroux, C. Cros, W. Gang, R. Kanno, M. Pouchard, *Solid State Ion.* **1985**, *15*, 293–300.
[31] M. Partik, H. D. Lutz', *Mater. Res. Bull.* **1997**, *32*, 1073–1078.
[32] N. Dubouis, T. Marchandier, G. Rousse, F. Marchini, F. Fauth, M. Avdeev, A. Iadecola, B. Porcheron, M. Deschamps, J. M. Tarascon, A. Grimaud, *Nat. Mater.* **2021**, *20*, 1545–1550.
[33] J. Liang, X. Li, J. T. Kim, X. Hao, H. Duan, R. Li, X. Sun, *Angew. Chem. Int. Ed.* **2023**, *135*, e202217081.
[34] J. Perl, J. Shin, J. Schümann, B. Faddegon, H. Paganetti, *Med. Phys.* **2012**, *39*, 6818–6837.
[35] K. Momma, F. Izumi, *J. Appl. Crystallogr.* **2011**, *44*, 1272–1276.
[36] A. L. Santhosha, L. Medenbach, J. R. Buchheim, P. Adelhelm, *Batter. Supercaps* **2019**, *2*, 524–529.
[37] S. Hori, R. Kanno, X. Sun, S. Song, M. Hirayama, B. Hauck, M. Dippon, S. Dierickx, E. Ivers-Tiffée, *J. Power Sources* **2023**, *556*, 232450.
[38] M. Wiche, Y. Yusim, K. Vettori, R. Ruess, A. Henss, M. T. Elm, *ACS Appl. Mater. Interfaces* **2024**, *16*, 3253–3259.
[39] M. Partik, M. Schneider, H. D. Lutz, *Z Anorg Allg Chem* **1994**, *620*, 791–795.
[40] S. Ohno, C. Rosenbach, G. F. Dewald, J. Janek, W. G. Zeier, *Adv. Funct. Mater.* **2021**, *31*, 2010620.
[41] G. F. Dewald, S. Ohno, M. A. Kraft, R. Koerver, P. Till, N. M. Vargas-Barbosa, J. Janek, W. G. Zeier, *Chem. Mater.* **2019**, *31*, 8328–8337.
[42] C. Rosenbach, F. Walther, J. Ruhl, M. Hartmann, T. A. Hendriks, S. Ohno, J. Janek, W. G. Zeier, *Adv. Energy Mater.* **2023**, *13*, 2203673.
[43] F. Liu, L. Gao, Z. Zhang, L. Zhang, N. Deng, Y. Zhao, W. Kang, *Energy Storage Mater.* **2024**, *64*, 103072.
[44] S. Samanta, S. Bera, R. K. Biswas, S. Mondal, L. Mandal, A. Banerjee, *ACS Energy Lett.* **2024**, *8*, 3683–3693.
[45] M. A. Kraft, S. P. Culver, M. Calderon, F. Böcher, T. Krauskopf, A. Senyshyn, C. Dietrich, A. Zevalkink, J. Janek, W. G. Zeier, *J. Am. Chem. Soc.* **2017**, *139*, 10909–10918.

Manuscript received: July 31, 2024

Revised manuscript received: October 3, 2024

Accepted manuscript online: October 16, 2024

Version of record online: November 21, 2024